Rapid Communications

Quantum phase diagram of a Moiré-Hubbard model

Haining Pan, Fengcheng Wu, and Sankar Das Sarma
Condensed Matter Theory Center and Joint Quantum Institute, Department of Physics, University of Maryland, College Park, Maryland 20742, USA

(Received 28 August 2020; revised 19 October 2020; accepted 20 October 2020; published 5 November 2020)

We theoretically study a generalized Hubbard model on Moiré superlattices of twisted bilayers, and find very rich filling-factor-dependent quantum phase diagrams tuned by interaction strength and twist angle. Strong long-range Coulomb interaction in the Moiré-Hubbard model induces Wigner crystals at a series of fractional filling factors. The effective lattice of the Wigner crystal is controlled by the filling factor, and can be triangle, rectangle, honeycomb, kagome, etc., providing a single platform to realize many different spin models on various lattices by simply tuning carrier density. In addition to Wigner crystals that are topologically trivial, interaction-induced Chern insulators emerge in the phase diagram. This finding paves a way for engineering interaction-induced quantum anomalous Hall effect in Moiré-Hubbard systems where the corresponding single-particle Moiré band is topologically trivial.

DOI: 10.1103/PhysRevB.102.201104

Introduction. Twisted bilayers with a long-period Moiré pattern provide versatile platforms to study strongly correlated physics, as many-body interactions are effectively enhanced in narrow Moiré bands. It has been theoretically proposed that a generalized Hubbard model can be simulated in twisted bilayers based on group-VI transition metal dichalcogenides (TMDs) [1,2], which have fewer low-energy degrees of freedom compared to twisted bilayer graphene [3–5] and therefore, allow quantum simulations of model Hamiltonians. Recent experiments [6–11] performed using a variety of techniques on twisted bilayer TMDs found compelling evidence of correlated insulators (CIs) not only at integer filling factors (i.e., one electron or hole per Moiré cell) but also at a series of fractional filling factors. The CIs at the integer filling factors are driven primarily by the on-site repulsion in the Hubbard model, while those at fractional filling factors are interpreted as generalized Wigner crystals [6,9–11] induced by the long-range Coulomb repulsion. The observed abundant correlated insulating states in twisted bilayer TMDs call for thorough theoretical investigations of this intriguing two-dimensional (2D) Moiré-Hubbard system.

In this Rapid Communication, we theoretically study a generalized Hubbard model on triangular Moiré lattice realized in twisted bilayer TMDs. We show that the quantum phase diagram at a given fractional filling factor contains a rich set of competing phases that can be tuned by the twist angle θ and the dielectric environment. We also find that the phase diagram depends nontrivially on the filling factor. When interaction is much greater than the kinetic energy, Wigner crystals generally form to minimize the long-range Coulomb interaction. The effective lattices of Wigner crystals depend sensitively on the filling factor, and can be triangle, rectangle, honeycomb, kagome, etc. After the electron spin degree of freedom is taken into account, spin models on distinct lattices can be simulated in this system by simply tuning the carrier density, leading to a variety of charge- and spin-ordered phases. In competition with these states derived from Wigner crystals, interaction-induced Chern insulators also appear in the phase diagram, which is remarkable since the noninteracting band structure in the model is topologically trivial. Here Chern insulators arise spontaneously from effective fluxes that are spontaneously generated either by nontrivial spin texture or by interaction-induced complex hopping phases. We elaborate our results by presenting calculated rich quantum phase diagrams at representative fractional filling factors, and discuss their experimental implications.

Model. We study a Moiré-Hubbard model defined as follows:

$$H = \sum_{s}\sum_{i,j} t_s(\boldsymbol{R}_i - \boldsymbol{R}_j) c^{\dagger}_{i,s} c_{j,s} + \frac{1}{2}\sum_{s,s'}\sum_{i,j} U(\boldsymbol{R}_i - \boldsymbol{R}_j) c^{\dagger}_{i,s} c^{\dagger}_{j,s'} c_{j,s'} c_{i,s}, \quad (1)$$

where $\boldsymbol{R}_i$ represents the position of site i in a triangular lattice formed in the Moiré pattern [Fig. 1(a)], s is the spin index, and t and U are, respectively, the hopping parameter and the interaction strength. As proposed in Refs. [1,2,12], the model in Eq. (1) can be simulated in twisted TMD heterobilayers as well as homobilayers. For definiteness, we use twisted homobilayer WSe_2 ($tWSe_2$) as the model system in this work, and Eq. (1) is then constructed following our previous work [12] for low-energy holes in the first Moiré valence band at $\pm K$ valleys. Here we use $c^{\dagger}_{i,s}$ to represent the hole operator, and $s = \uparrow$ and $\downarrow$ are locked to $+K$ and $-K$ valleys, respectively. We define a filling factor ν as $(1/\mathcal{N})\sum_{i,s} c^{\dagger}_{i,s} c_{i,s}$, which counts the number of holes per Moiré cell ($\mathcal{N}$ is the total number of Moiré sites in the system). The charge neutrality point of the semiconducting twisted bilayer corresponds to $\nu = 0$. For simplicity, we assume that no external out-of-plane displacement field is applied to WSe_2, and then the model in Eq. (1) respects emergent spin SU(2) symmetry

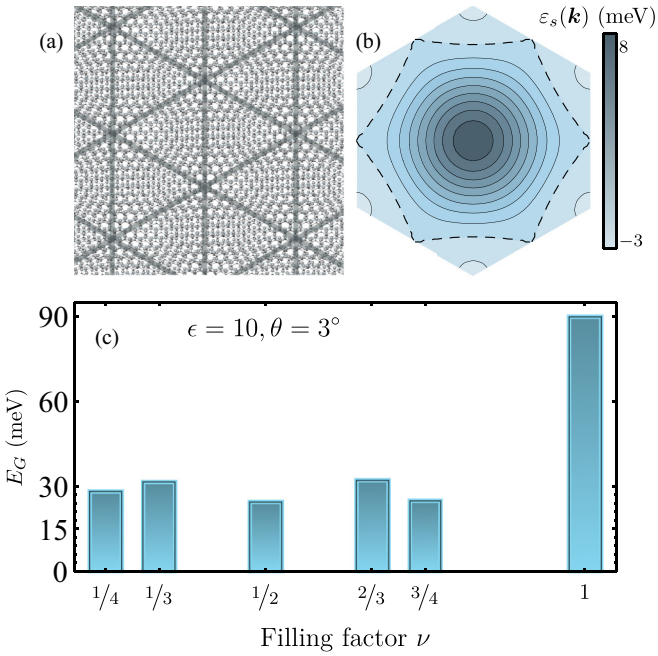

FIG. 1. (a) The effective triangular lattice formed in the Moiré pattern. (b) The single-particle Moiré band $\varepsilon_s(\boldsymbol{k})$ of Eq. (1) at $\theta = 3°$, where s can be $\uparrow$ or $\downarrow$. The dashed line marks the contour at the van Hove energy. (c) The correlated insulating gap at representative rational filling factors ν.

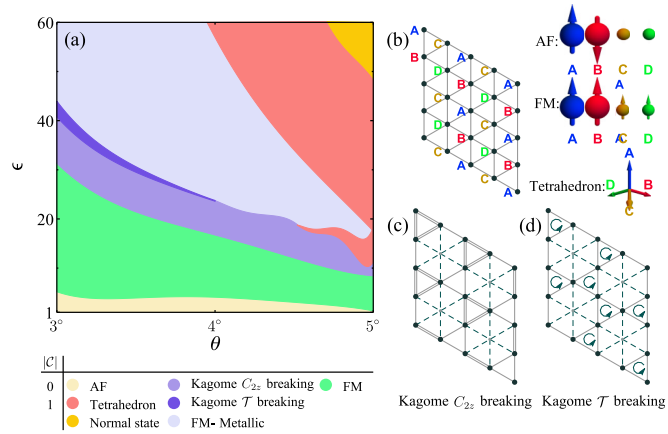

FIG. 2. (a) The quantum phase diagram at $\nu = 1/2$ as a function of θ and ϵ. Some phases are illustrated in (b)–(d). (b) In the AF and FM phases, A and B sublattices are dominantly occupied, while C and D sublattices are less occupied. In the AF phase, spin polarization is antiparallel on A and B, but vanishes on C and D. In the FM phase, all sites have parallel spin polarization but different densities. In the tetrahedron phase, the four sublattices have equal density but different spin orientations that extend a solid angle of 4π. (c) and (d) show the kagome phases with C_{2z} and $\mathcal{T}$ symmetry breaking, respectively.

and C_6 point-group symmetry. An important advantage of the Moiré platform is that both the hopping parameters and the interaction strength are highly tunable. Generally speaking, the Moiré bandwidth becomes narrower at smaller twist angle (larger Moiré period) and many-body interaction effects become more prominent [1,2,13]. We show the twist-angle dependence of t and U in the Supplemental Material [14] (see, also, Refs. [15,16] therein). In the calculation of U, we project a screened Coulomb interaction $(e^2/\epsilon)(1/r - 1/\sqrt{r^2 + d^2})$ to the low-energy Moiré states, where ϵ is the background dielectric constant that is tunable by the dielectric environment and $d/2$ is the distance between the Moiré system and a nearby metallic gate. We take ϵ as a free parameter and d, which is also experimentally controllable, to be 60 nm in calculations.

We perform self-consistent mean-field (MF) Hartree-Fock studies of the Moiré Hubbard model at representative filling factors with a variety of initial ansatze that range from Wigner crystals (which can be derived from the classical Coulomb model [14]) to topological states. At a given fractional filling factor, we generally find multiple solutions to the Hartree-Fock equation, and their energetic competitions give rise to rich quantum phase diagrams. An overview of our results is illustrated in Fig. 1(c) showing the interaction-induced gap E_G at rational ν with a denominator up to 4. In our theory, the CI at the integer filling $\nu = 1$ is a Mott insulator, and its gap is primarily determined by the on-site repulsion [12]. CIs at fractional fillings often require the presence of off-site repulsion and generally have smaller charge gaps. The relative trend of our calculated E_G in Fig. 1 as a function of ν agrees well with a recent experiment in Ref. [9], which provides confidence in the validity of our theory.

$\nu = 1/2$. The quantum phase diagram at $\nu = 1/2$ is shown in Fig. 2(a), which displays six symmetry-breaking phases (besides a normal state without symmetry breaking) as a function of θ and ϵ. When interaction is strong (small ϵ), a Wigner crystal with a stripe charge-density wave (CDW) forms [Fig. 2(b)], and hosts a coupled-chain spin Heisenberg model. Our MF results show that the Heisenberg model has an antiferromagnetic (AF) exchange coupling, as an AF phase has a lower energy compared to the ferromagnetic (FM) phase for small ϵ. When interaction decreases by increasing ϵ, the stripe CDW gradually weakens and the FM phase becomes energetically more favorable. Therefore, charge and spin orderings are closely related. By further decreasing the interaction strength, CDW can completely disappear but the FM ordering can remain, which leads to a FM metallic phase.

In addition to these relatively simple charge- and spin-ordered phases, we also find three more exotic phases in Fig. 2(a): one tetrahedron phase and two kagome phases. In the tetrahedron phase, there is spin ordering but no charge ordering. The spin texture on the four magnetic sublattices forms a tetrahedron, which leads to a real-space Berry flux of π for electronic motion along each triangular plaquette. We numerically verify that the tetrahedron phase is a Chern insulator with a Chern number of $|\mathcal{C}| = 1$. This phase arises because our noninteracting Moiré band at $\nu = 1/2$ is close to the van Hove energy, and the corresponding Fermi surface is close to nesting [Fig. 1(b)], which leads to an instability towards noncollinear ordering [17]. In agreement with this weak-coupling picture, we find that the tetrahedron phase appears at relatively weak interactions.

In the two kagome phases shown in Figs. 2(c) and 2(d), charge ordering leads to an effective kagome lattice where one out of four triangular sites are nearly unoccupied, and the other three sites each have a site occupancy $\sim 2/3$ and nearly

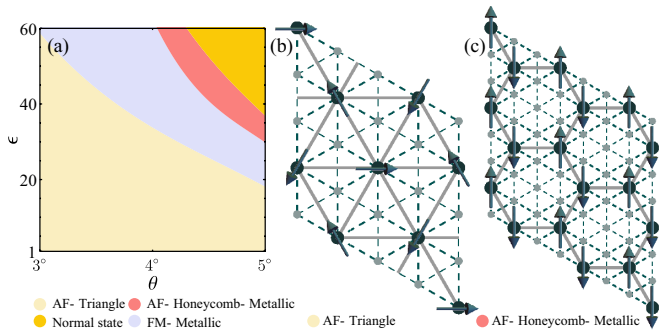

FIG. 3. (a) The quantum phase diagram at $\nu = 1/3$. Two of the phases are illustrated in (b) and (c).

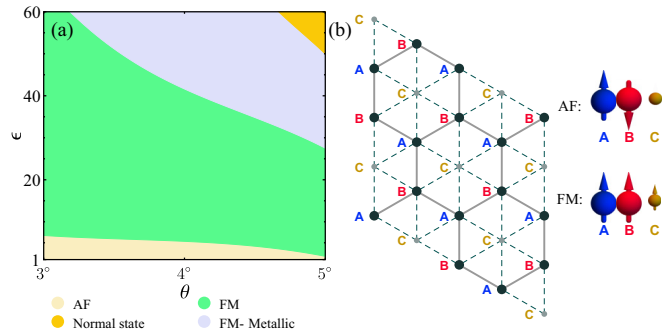

FIG. 4. (a) The quantum phase diagram at $\nu = 2/3$. (b) AF and FM phases on an effective honeycomb lattice.

full spin polarization. This spin- and charge-ordered kagome phase would host Dirac cones in the mean-field quasiparticle band structure at the Fermi energy, if there was no additional symmetry breaking. However, the Dirac cones can be gapped out by further breaking either twofold rotation C_{2z} symmetry or time-reversal $\mathcal{T}$ symmetry.

In the C_{2z}-breaking kagome phase, the interaction-renormalized effective hopping parameters from a site to its nearest neighbors on opposite directions become different but remain real [Fig. 2(c)], which leads to a valence bond solid insulator that is topologically trivial. In the other phase with $\mathcal{T}$ breaking, the effective hopping parameters acquire complex phases with a pattern shown in Fig. 2(d). This $\mathcal{T}$-breaking kagome phase with spontaneously induced fluxes of ϕ in the triangles and -2ϕ in the hexagons is analogous to the Haldane model on honeycomb lattice [18], and is a Chern insulator with $|\mathcal{C}| = 1$ [14]. The topological kagome phase arising from a generalized Hubbard model on a triangular lattice has not been reported previously and provides a new mechanism to realize quantum anomalous Hall effect in a realistic experimental system.

$\nu = 1/3$. In the quantum phase diagram at $\nu = 1/3$ shown in Fig. 3(a), the Wigner crystal with a $\sqrt{3} \times \sqrt{3}$ CDW is robust up to very large ϵ, and 120° AF order with a 3×3 period develops on top of this Wigner crystal [Fig. 3(b)]. For weak interactions, we find two metallic phases in addition to the normal state: (1) a FM metallic phase with spin polarization but no CDW; (2) an AF metallic phase [Fig. 3(c)] with a 3×3 CDW, where sites with dominant occupancy form an effective honeycomb lattice and host collinear AF ordering.

$\nu = 2/3$. The Wigner crystal at $\nu = 2/3$ is dual to that at $\nu = 1/3$, and forms a honeycomb lattice (Fig. 4), where spins develop collinear AF order in the strong interaction limit as expected from an effective Heisenberg model. By decreasing interaction, there is a transition from AF to FM spin orderings with the same $\sqrt{3} \times \sqrt{3}$ CDW, and then to FM without CDW, and finally to the normal state. We note that topological states derived from the Haldane model [18] can be Hartree-Fock solutions at both $\nu = 1/3$ and $2/3$, but they are not energetically favorable within our explored parameter space [14].

$\nu = 1/4$. At $\nu = 1/4$, there are two types of Wigner crystals: (1) a 2×2 triangular phase; and (2) a stripe phase with a $2 \times \sqrt{3}$ rectangular superlattice, where the former appears in most of the parameter space in the phase diagram [Fig. 5(a)] and the latter forms for small ϵ and large θ. In both phases, the effective spin exchange interaction is weak because of the large separation (small hopping) between the primarily occupied sites, and therefore, AF and FM spin orderings closely compete in energy. We also find a Chern insulator state at $\nu = 1/4$ that is analogous to the $\nu = 1/2$ kagome phases with $\mathcal{T}$ symmetry breaking, but it is energetically unfavorable [14].

$\nu = 3/4$. We find seven symmetry-breaking phases in the phase diagram at $\nu = 3/4$, as shown in Fig. 6(a). For $\epsilon < 5$, we find two types of Wigner crystals: (1) a kagome lattice [Fig. 6(b)] for $\theta < 4.2°$, and (2) an antistripe lattice [Fig. 6(d)] for $\theta > 4.2°$, which are, respectively, dual to the 2×2 triangular and $2 \times \sqrt{3}$ stripe Wigner crystals at $\nu = 1/4$. We find that AF spin ordering has lower energy compared to FM spin ordering on both the kagome and antistripe lattices for $\epsilon < 5$. It is important to note that both lattices with AF spin exchange couplings are frustrated and can host a large number of degenerate classical magnetic ground states, which could lead to quantum spin liquid states when quantum fluctuations in the spin sector are taken into account.

For $\epsilon > 5$, we find a FM phase on the kagome lattice, and the associated CDW gradually melts as ϵ increases, and

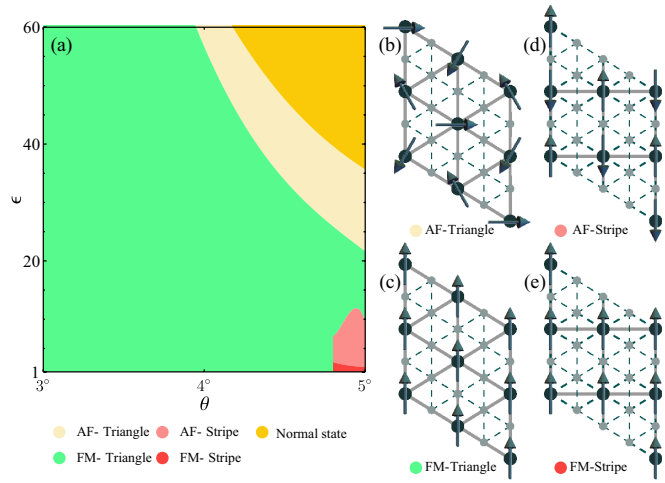

FIG. 5. (a) The quantum phase diagram at $\nu = 1/4$. (b) 120° AF and (c) FM spin structures on the 2×2 triangular Wigner crystal. (d) Collinear AF and (e) FM spin structures on the $2 \times \sqrt{3}$ stripe Wigner crystal.

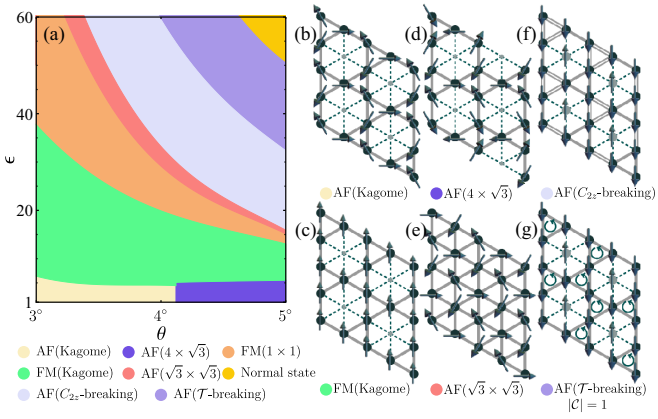

FIG. 6. (a) The quantum phase diagram at $\nu = 3/4$. (b) AF and (c) FM spin structures on a kagome Wigner crystal. (d) AF spin structure on an antistripe Wigner crystal. The AF spin structures shown in (b) and (d) are mean-field results, and may not be the actual ground states because of fluctuations. (e) 120° AF state without charge-density wave. (f) and (g) Sites with spin-up (down) polarization form triangular (kagome) lattice. In (f), C_{2z} symmetry is spontaneously broken, which leads to a valence bond solid insulator. In (g), $\mathcal{T}$ symmetry is spontaneously broken due to interaction-induced effective flux, which leads to a Chern insulator.

finally vanishes, leading to a FM 1×1 phase without CDW. In competition with this FM 1×1 phase, there is a 120° AF phase that has only spin-density wave but no CDW, as illustrated in Fig. 6(e).

Finally, we find two collinear AF phases that are derived from the kagome phases at $\nu = 1/2$. Noting that $3/4 = 1/4 + 1/2$, we can construct collinear AF phases with effective filling factors of $1/4$ for the spin $\uparrow$ sector and $1/2$ for the spin $\downarrow$ sector. Spin $\uparrow$ and $\downarrow$ states, respectively, occupy sites on kagome and triangular lattices that are dual to each other. On the kagome lattice formed by spin $\downarrow$ states, C_{2z} or $\mathcal{T}$ symmetry can be further broken, as in the case of $\nu = 1/2$, leading to the two AF phases illustrated in Figs. 6(f) and 6(g) that are respectively topologically trivial and nontrivial [14].

Discussions. Our MF results should be taken to be qualitative instead of quantitative, as Hartree-Fock theory generally overestimates the tendency towards ordering. However, the advantage of MF theory is that it allows construction of a very large family of possible ground state candidate phases. We envision that more sophisticated numerical approaches can be applied to the Moiré Hubbard model, which could verify intriguing phases such as Chern insulators predicted by our theory and unveil more exotic phases, for example, spin liquid states on the effective kagome lattice at $\nu = 3/4$, but such numerical methods are extremely computationally demanding and therefore, detailed results as functions of filling factors, interaction strength, and twist angle as provided in our work are challenging. It is useful to mention here for comparison that the MF theory applied on the standard 2D minimal square-lattice on-site Hubbard model only finds a few phases (AF, FM, paramagnet, and spiral) as functions of interaction and filling [19,20]. Due to space limit, we only present phase diagrams at rational ν with a denominator up to 4, but we do also find correlated insulators at other fractional filling factors.

The predicted rich phase diagrams can lead to very rich experimental phenomena, because different phases can be accessed by tuning experimentally controllable parameters (e.g., θ and ϵ). Current experiments [6–11] were all performed using hexagonal boron nitride as encapsulating material. The corresponding dielectric constant ϵ is about 5–10. For this range of ϵ, our calculations show that ground states at the fractional filling factors are Wigner crystals. The effective lattice of Wigner crystals can spontaneously break threefold rotational symmetry, particularly in stripe phases at $\nu = 1/2$ and $1/4$, which can be probed optically using linear dichroism [10]. To realize the predicted Chern insulators at $\nu = 1/2$ and $3/4$, weaker interaction (i.e., $\epsilon > 10$) is desirable, which can be engineered by changing the dielectric environment, for example, using an encapsulating material with a higher dielectric constant and reducing the distance from the sample to the metallic gate. Experimental observation of such interaction-induced Chern insulators in a system with topologically trivial single-particle bands would greatly enhance the scope of quantum anomalous Hall effect.

Acknowledgments. This work is supported by the Laboratory for Physical Sciences.

[1] F. Wu, T. Lovorn, E. Tutuc, and A. H. MacDonald, Phys. Rev. Lett. **121**, 026402 (2018).
[2] F. Wu, T. Lovorn, E. Tutuc, I. Martin, and A. H. MacDonald, Phys. Rev. Lett. **122**, 086402 (2019).
[3] R. Bistritzer and A. H. MacDonald, Proc. Natl. Acad. Sci. USA **108**, 12233 (2011).
[4] Y. Cao, V. Fatemi, S. Fang, K. Watanabe, T. Taniguchi, E. Kaxiras, and P. Jarillo-Herrero, Nature (London) **556**, 43 (2018).
[5] Y. Cao, V. Fatemi, A. Demir, S. Fang, S. L. Tomarken, J. Y. Luo, J. D. Sanchez-Yamagishi, K. Watanabe, T. Taniguchi, E. Kaxiras, R. C. Ashoori, and P. Jarillo-Herrero, Nature (London) **556**, 80 (2018).
[6] E. C. Regan, D. Wang, C. Jin, M. I. Bakti Utama, B. Gao, X. Wei, S. Zhao, W. Zhao, Z. Zhang, K. Yumigeta, M. Blei, J. D. Carlström, K. Watanabe, T. Taniguchi, S. Tongay, M. Crommie, A. Zettl, and F. Wang, Nature (London) **579**, 359 (2020).
[7] Y. Tang, L. Li, T. Li, Y. Xu, S. Liu, K. Barmak, K. Watanabe, T. Taniguchi, A. H. MacDonald, J. Shan, and K. F. Mak, Nature (London) **579**, 353 (2020).
[8] L. Wang, E.-M. Shih, A. Ghiotto, L. Xian, D. A. Rhodes, C. Tan, M. Claassen, D. M. Kennes, Y. Bai, B. Kim, K. Watanabe, T. Taniguchi, X. Zhu, J. Hone, A. Rubio, A. Pasupathy, and C. R. Dean, Nat. Mater. **19**, 861 (2020).
[9] Y. Xu, S. Liu, D. A. Rhodes, K. Watanabe, T. Taniguchi, J. Hone, V. Elser, K. F. Mak, and J. Shan, arXiv:2007.11128.

[10] C. Jin, Z. Tao, T. Li, Y. Xu, Y. Tang, J. Zhu, S. Liu, K. Watanabe, T. Taniguchi, J. C. Hone, L. Fu, J. Shan, and K. F. Mak, arXiv:2007.12068.
[11] X. Huang, T. Wang, S. Miao, C. Wang, Z. Li, Z. Lian, T. Taniguchi, K. Watanabe, S. Okamoto, D. Xiao, S.-F. Shi, and Y.-T. Cui, arXiv:2007.11155.
[12] H. Pan, F. Wu, and S. Das Sarma, Phys. Rev. Research **2**, 033087 (2020).
[13] M. H. Naik and M. Jain, Phys. Rev. Lett. **121**, 266401 (2018).
[14] See Supplemental Material at http://link.aps.org/supplemental/10.1103/PhysRevB.102.201104 for calculation details.
[15] T. Fukui, Y. Hatsugai, and H. Suzuki, J. Phys. Soc. Jpn. **74**, 1674 (2005).
[16] R. Yu, X. L. Qi, A. Bernevig, Z. Fang, and X. Dai, Phys. Rev. B **84**, 075119 (2011).
[17] I. Martin and C. D. Batista, Phys. Rev. Lett. **101**, 156402 (2008).
[18] F. D. M. Haldane, Phys. Rev. Lett. **61**, 2015 (1988).
[19] J. E. Hirsch, Phys. Rev. B **31**, 4403 (1985).
[20] P. A. Igoshev, M. A. Timirgazin, V. F. Gilmutdinov, A. K. Arzhnikov, and V. Y. Irkhin, J. Phys.: Condens. Matter **27**, 446002 (2015).